Phase behavior of ultra-soft spheres shows stable bcc lattices

A. Scotti,[1] J. E. Houston,[2] M. Brugnoni,[1] M. M. Schmidt,[1] M. F. Schulte,[1]
S. Bochenek,[1] R. Schweins,[3] A. Feoktystov,[4] A. Radulescu,[4] and W. Richtering[1,5]

[1]*Institute of Physical Chemistry, RWTH Aachen University, 52056 Aachen, Germany*
[2]*European Spallation Source ERIC, Box 176, SE-221 00 Lund, Sweden*
[3]*Institut Laue-Langevin ILL DS/LSS, 71 Avenue des Martyrs, F-38000 Grenoble, France*
[4]*Forschungszentrum Jlich GmbH, Jülich Centre for Neutron Science*
JCNS at Heinz Maier-Leibnitz Zentrum MLZ, 85748 Garching, Germany
[5]*JARA-SOFT, 52056 Aachen, Germany*

(Dated: October 1, 2020)

The phase behavior of super-soft spheres is explored using solutions of ultra-low crosslinked poly(*N*-isopropylacrylamide) based microgels as a model system. For these microgels, the effects of the electric charges on their surfaces can be neglected and, therefore, only the role of softness on the phase behavior is investigated. The samples show a liquid-to-crystal transition at higher volume fraction with respect to both hard spheres and stiffer microgels. Furthermore, stable body centered cubic (bcc) crystals are observed in addition to the expected face centered cubic (fcc) crystals. Small-angle X-ray and neutron scattering with contrast variation allow the characterization of both the microgel-to-microgel distance, and the architecture of single microgels in crowded solutions. The measurements reveal that the stable bcc crystals depend on the interplay between the collapse and the interpenetration of the external shell of the ultra-low crosslinked microgels.

Colloidal dispersions are a suitable model system to reproduce the behavior of atomic systems and complex fluids. For instance, the possibility to have entropy-driven phase transitions was largely debated in condensed matter community and was only predicted theoretically [1–3]. The entropy-driven formation of crystals was first proven by Pusey and van Megen in the late 1980s using a solution of polymethylmethacrylate (PMMA) hard spheres [4]. From this moment, colloidal dispersions have been largely used to explore phase transitions both in two- and three-dimensions [5–8]. The aforementioned studies used suspensions of hard incompressible colloids, which were sterically stabilized.

At the same time of the experiments of Pusey and van Megen, Pelton and Chibante synthesized monodisperse spherical crosslinked polymeric networks based on the monomer *N*-isopropylacrylamide (NIPAM) [9]. The resultig pNIPAM-based microgels have been largely used to explore phase transition and flow properties of soft spheres due to their colloidal size and intrinsic softness [10–18]. Indeed softness, that is the capability to deswell, deform or interpenetrate, has a strong impact on the phase transitions and rheological properties of solutions of spheres. For instance, the boundary of the transition between liquid and crystalline phases are shifted to higher concentrations [19] as predicted by computer simulations [20]. Furthermore, size polydispersity suppresses the crystallization of hard spheres when it is as high as 12%. In contrast, solutions of soft microgels can crystallize even when the nominal size polydispersity is close to 20% [13]. This is due to the capability of microgels to adjust their size in response to variations in the osmotic pressure of the solution [18]. In particular, larger microgels deswell first and fit into lattices composed of the smallest microgels without giving rise to defects [21, 22].

It is worth noting that even if pNIPAM-based microgels are usually referred to as neutral, a significant amount of charges are incorporated at the microgel's periphery due to initiator fragments [23]. These charges, and the corresponding ions, play a fundamental role in determining the swelling behavior of microgels in concentrated solutions as shown both by experiments [13, 18] and computer simulations [24, 25].

Therefore, to study the phase behavior of truly neutral soft spheres the number of charges on the microgel's surface has to be minimized. This can be achieved using the so-called ultra-low crosslinked (ULC) microgels that are synthesized without the addition of crosslinker agents during the precipitation polymerization. The networks are formed *via* atom abstraction reactions during the polymerization of NIPAM initiated with a peroxydisulfat initiator [26]. During the synthesis of ULC microgels, many polymeric chains, and the associated charged fragments of the initiators, precipitate in the polymer globules, but are not chemically attached to the network. These chains are washed out of the microgels during purification, which is confirmed by the very low yield of the precipitation polymerization of ULC microgels ($\approx 10\%$) compared to the yield of regularly crosslinked microgels ($\approx 90\%$). This means that the ULC microgels incorporate a lower amount of polymeric chains, and associated charges, with respect to microgels synthesized with the use of a crosslinker [27, 28]. The lower surface charge of ULC microgels with respect to microgels synthesized with the addition of crosslinker is confirmed by measurements of their electrophoretic mobility shown in the *Supplemental Material* in Table S1. For these reasons we can consider ultra-low crosslinked microgels as almost neutral soft spheres. Details on the synthesis and the characterization of the swelling behavior of the ultra-low crosslinked microgels used in this study with dynamic light scattering can be found in the *Supplemental Mate-*

rial in Figure S1.

Due to their poorly crosslinked network, ULC microgels show a more pronounced deswelling behavior when embedded in a matrix of regularly crosslinked, stiffer microgels [28]. Furthermore, their bulk rheological properties present common features with both hard spheres and flexible macromolecules, depending on the concentration of the solution [29]. This particle-to-polymer transition is also prominent when these ULC microgels are confined to an interface: the dominance of their polymeric or particle-like nature depends on both their concentrations [27] and the adsorption procedures [30].

In this study, we use solutions of ULC microgels to explore the phase behavior of soft spheres. The liquid-to-solid phase transition is shifted to higher generalized volume fraction with respect to both hard spheres and conventionally cross-linked microgels. Furthermore, the phase behavior shows a stable body centered cubic (bcc) lattice, which is not observed for other colloids. The coexistence of bcc lattice with face centered cubic (fcc) lattice, expected for hard spheres and other microgels, is rationalized by means of small-angle scattering experiments. We probe both the microgel-to-microgel arrangement in solution (X-rays, SAXS) and the structure of the single microgels as a function of concentration (neutrons, SANS with contrast variation). The comparison between the results of these techniques shows that bcc crystals appear in the concentrations area where the collapse of the microgels competes with their capability to interpenetrate their neighbors.

I. PHASE BEHAVIOR

At constant temperature and pressure, the quantity that determines the phase behavior of solutions of microgels is the volume occupied by the microgels in the solution, this is the volume fraction. In contrast to hard spheres that have a well-defined border and, therefore, volume, microgels have a fuzzy periphery that makes it hard to define their volume. It is well accepted that a generalized volume fraction can be used to describe the packing density of soft microgels [31–34]:

$$\zeta = \frac{N V_{sw}}{V_{tot}}\,; \tag{1}$$

where V_{tot} is the volume of the solution and N and V_{sw} are the number and the volume of the microgels in diluted solution, respectively. ζ is connected to the weight concentration *via* a constant that can be obtained by measuring the viscosity of highly diluted solutions of microgels [19, 35]. This method is also valid to determine the generalized volume fraction of ULC microgels [29].

A series of samples have been realized by successive dilution, starting from a microgel solution with $\zeta = 1.50 \pm 0.02$. The starting solution was prepared adding bi-distilled water to the microgel powder obtained from the lyophilization of the purified solution resulting from the synthesis (*Supplemental Material*). The weight concentrations have been converted into generalized volume fractions using the conversion constant obtained from viscosity measurements, $K = 44.9 \pm 0.01$, Figure S2. The series of samples covers a range of ζ between 0.354 ± 0.006 and 1.50 ± 0.02.

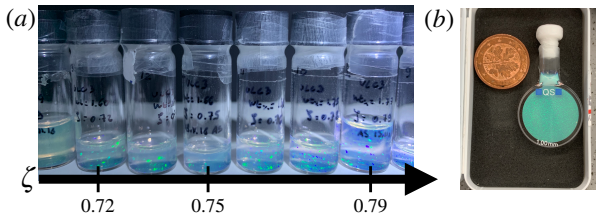

FIG. 1. (a) Solutions of ultra-low crosslinked microgels with increasing generalized volume fraction, ζ, from left to right. (b) Solution composed by a mixture of deuterated and hydrogenated ($\zeta_H = 0.080 \pm 0.003$) ULC microgels at $\zeta = 0.750 \pm 0.009$. The iridescence due to the Bragg peaks is visible in crystalline samples. All samples were stored at 20.0 ± 0.5 °C.

The crystals formed in the solutions of ULC microgels are clearly visible by eye as green spots in Figure 1(a). Crystals are not visible up to a concentration of $\zeta_f = 0.717 \pm 0.09$ where they appear at the bottom of the vials and coexistence between crystals and liquid is observed. ζ_f is known as freezing point. With increasing ζ, the volume fraction of the solutions occupied by crystals increases linearly [12] until $\zeta_m = 0.744 \pm 0.009$. For this volume fraction, crystals are present in the entire volume of the solution. ζ_m is called melting point.

The values of ζ_f and ζ_m are significantly larger than the values usually observed for the freezing- and melting points of solutions of microgels synthesized with the addition of crosslinker agents (referred to as regular microgels in the following): 0.56 and 0.61, respectively [13, 19, 34, 36, 37]. Computer simulations have shown that the shift of the boundaries of these phase transitions is related to a softer interaction potential acting between the microgels in solution [1, 20].

The fact that ζ_f and ζ_m are at values larger than those for regular microgels indicates that the interaction between ULC microgels is softer. This fact is further confirmed by the increase of the elastic modulus of the solutions of ULC microgels with ζ. The black squares in Figure 2 are the values of G_p, the plateau of the elastic modulus, measured with oscillatory frequency sweep. Recently, it has been shown that a correct description of the microgel-to-microgel interaction can be achieved using a phenomenological multi-Hertzian model, [38] that depends on the concentration regime and, therefore, on the different length-scales that characterize the microgels [32, 39]. However, a simple but instructive method to compare the softness of the microgel-to-microgel interaction is to assume a potential of the form $U(r) \sim r^{-n}$.

When the potential has this form, the dependence of G_p on ζ is: $G_p \sim \zeta^{(1+n/3)}$.

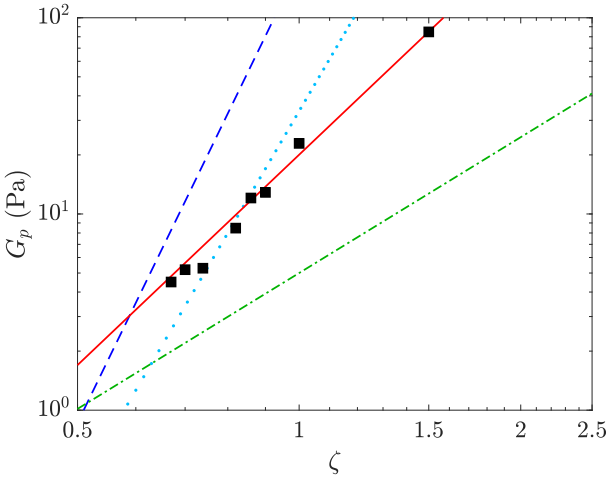

FIG. 2. Values of the plateau of the elastic modulus of solutions of ultra-low crosslinked microgels, G_p, versus generalized volume fraction, ζ (black squares). The red line represents the fit of the data using $G_p \sim \zeta^{(1+n/3)}$. The dashed, dotted and dash-dotted lines represent the increase of G_p as a function of ζ for 10 mol%, 1 mol% crosslinked microgels and linear polymer, respectively [27, 29].

For the ULC microgels used here, a fit of the data in Figure 2 leads to estimate $n_{ULC} = 7.7 \pm 0.2$. Following the computer simulations in Refs. [1] and [20], the value of n_{ULC} leads to a prediction for the freezing point at 0.70 of the packing fraction, in excellent agreement with our system that has $\zeta_f = 0.717 \pm 0.09$.

$n_{ULC} = 7.7 \pm 0.2$ is comparable to the values obtained for other solutions of ULC microgels [27, 29]. This value is significantly lower with respect to the exponent found for crosslinked microgels. As a comparison, the dashed and dotted lines represent the course of 10 mol% and 1 mol% crosslinked microgels, respectively, [27, 29] that have a $n \sim 20$. As a further comparison to the ULC microgels, the course for linear polymer is shown by the dash-dotted line, $n_{poly} = 2.3$ [40]. Figure 2 highlights that the ULC microgels interact with a microgel-to-microgel potential softer than regular microgels but still harder than linear polymers.

II. STRUCTURE FACTOR ANALYSIS: SMALL-ANGLE X-RAY SCATTERING

A more detailed characterization of the structures of the concentrated solutions, shown in Figure 1(a), has been achieved using small-angle X-ray scattering. In these experiments the scattered intensity, $I(q)$, is proportional to the product between the form factor, $P(q)$, and the structure factor, $S(q)$, which equals 1 in the limit of infinite dilution. The form factor contains all the information (size, polydispersity, shape, internal architecture) about the single scattering object. The structure factor depends on the particle-to-particle arrangement.

A. Detector images

The images of the SAXS detector are shown in Figure 3. The different panels correspond to the different generalized volume fractions of the solutions. The black circle in the center of all the images is the mask used to cover the forward scattering of the direct beam in close proximity to the beamstop. In all the images a light blue circle is visible. This corresponds to the values of the scattering vector, q, where it is most likely to find a microgel, in real space this is the nearest neighbor distance, d_{nn}. With increasing concentration from 0.498 ± 0.004, panel 3(a), to 1.20 ± 0.02, panel 3(i), the radius of this circle increases. This corresponds to an increase of the scattering vector and, therefore, a decrease of d_{nn}.

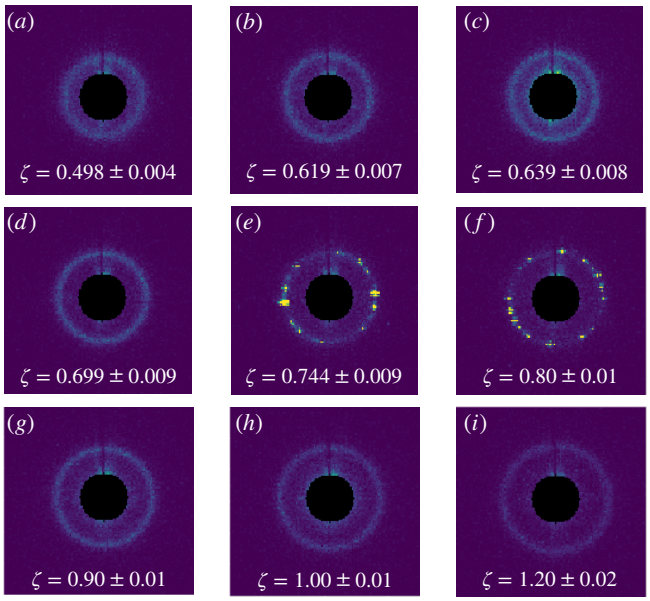

FIG. 3. Detector images acquired by SAXS measuring solutions of microgels with increasing generalized volume fraction (ζ) from panel (a) to (i). All samples have been measured at $T = 20.0 \pm 0.1$ °C.

Two examples of the scattering patterns of crystalline samples are shown in panels 3(e) and 3(f). Yellow spots, which correspond to higher intensity, are clearly visible over the underlying light blue circles. These dots are due to the scattering from the ordered lattices formed by the microgels. The presence of multiple dots relatively close to each other indicates that the samples present many poly-crystalline domains with different orientations. Furthermore, the absence of a second ring of Bragg peaks indicates that these crystals are small and the order is limited to short length scales. Indeed, the absence of

higher Bragg reflections has been reported in the literature for both microgels and hard sphere suspensions to be related to the presence of defects in the crystalline lattice mainly due to size mismatch between the particles forming the crystals [13, 41].

B. Intensities and structure factors

Figure 4 shows a series of $I(q)$ for samples at different concentrations, from $\zeta = 0.639 \pm 0.008$ (bottom) to $\zeta = 1.20 \pm 0.02$ (top). Data are shifted in the y-direction for clarity. These curves are obtained performing a 2D-integration of the images shown in Figure 3, and have been background subtracted. The first observation is that in all the curves there is a clear peak corresponding to the light blue circles observed in Figure 3. These peaks shift to higher q, that is smaller nearest-neighbor distance (d_{nn}), with increasing the concentration of microgels in solution (from bottom to top). For liquid and glassy samples, $d_{nn} \approx 2\pi/q_{max}$, with q_{max} the value of q corresponding to the maximum of the first peak [31, 42]. For crystalline lattices, d_{nn} depends on the lattice constant, but this relation is different for different crystalline lattices. For instance, with a the lattice constant, $d_{nn} = a/\sqrt{2}$ for a face centered cubic (fcc) lattice, while for a body centered cubic crystal $d_{nn} = a\sqrt{3}/2$.

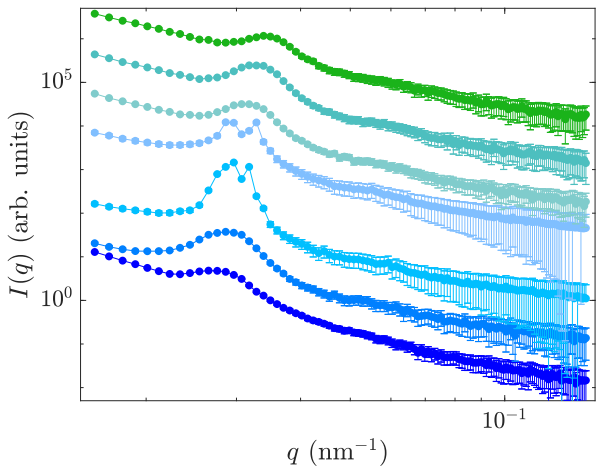

FIG. 4. SAXS intensities, $I(q)$, versus scattering vector, q, of solutions of microgels with increasing concentration from bottom to top: $\zeta = 0.639 \pm 0.008$; $\zeta = 0.699 \pm 0.009$; $\zeta = 0.744 \pm 0.009$; $\zeta = 0.80 \pm 0.01$; $\zeta = 0.90 \pm 0.01$; $\zeta = 1.00 \pm 0.01$; $\zeta = 1.20 \pm 0.02$. Data are shifted in the y-direction for clarity.

The peaks of the third and fourth $I(q)$s from the bottom corresponds to the panels 3(e) and 3(f). The data clearly show Bragg peaks detected in the scattering experiment. As noted above, only first order peaks are visible. This indicates that on one hand on short length scales the samples are strongly ordered, and on the other hand at larger length scales the order is lost: the crystals are relatively small and poly-crystalline samples form with defects in the lattice [13, 41].

Structure factors $S(q)$ are obtained by dividing the measured intensities, $I(q)$, by the SAXS intensity of the ULC microgels measured in diluted solutions ($\zeta < 0.05$) that is proportional to the form factor $P(q)$ of the ultra-low crosslinked microgels. This means that we are neglecting the possible deswelling/deformation of the microgels at high packing fractions. Nevertheless, it has been shown that this approach leads only to an error of $\ll 5\%$ [13, 18]. Since we are mainly interested in the features of the first peak this procedure is therefore appropriate.

C. Structure factor of disordered samples

Figure 5 shows the structure factors of the concentrated microgel solutions. We notice that, as expected, all the structure factors (blue squares) reach the plateau value of 1 (black horizontal lines) for high q.

The first two panels show the structure factors of liquid samples at packing fractions $\zeta = 0.4980 \pm 0.004$ and $\zeta = 0.619 \pm 0.007$, Figures 5(a) and 5(b), respectively. The red lines represent fits of the data with the Percus-Yevick structure factor [43] where the microgel generalized packing fraction, ζ_{PY}, and the radius of the microgels are fitting parameters. The fits have been performed using SASview 4.2.2 software. This model has already been used to describe solutions of compressible microgels at low packing fraction [17, 44, 45]. It is clear that while the position and the intensity of the first peak of the structure factor is well reproduced by the model, the data are not reproduced for high q. This may be due to the rapid decrease of the order in the samples and to the fact that we are neglecting changes in the form factor depending on concentration. Other factors that can lead to this disagreement between the data and the model are the low contrast of the ULC microgels and the fact that the Percus-Yevick structure factor we are using is aimed for low concentrated solutions of hard spheres [46]. Nevertheless, the values obtained for the generalized volume fraction ζ_{PY} are consistent with the value of ζ obtained from viscosity measurements (*Supplemental Material*, Figure S3). Furthermore, the nearest neighbor distance obtained from the fits are in good agreement with the d_{nn} obtained from q_{max}.

D. Structure factor of crystalline samples

The panels from 5(c) to 5(f) correspond to the structure factors of the crystalline samples. As mentioned above, we notice that only the first Bragg peaks are visible, revealing the presence of small poly-crystalline domains with different orientations within the samples and with a significant number of defects in the different lattices [13, 41]. The vertical red lines represent the ex-

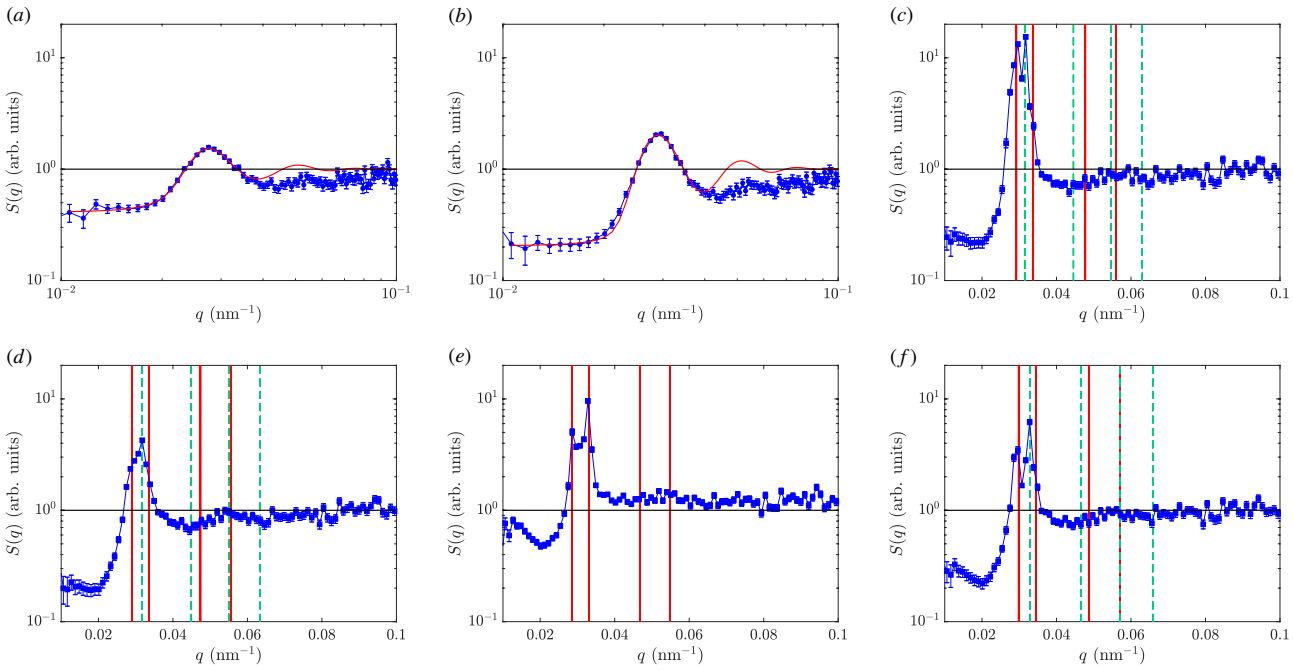

FIG. 5. Structure factor (blue squares) of solutions of ultra-low crosslinked microgels at packing fractions equal to: (a) $\zeta = 0.4980 \pm 0.004$, (b) $\zeta = 0.619 \pm 0.007$, (c) $\zeta = 0.744 \pm 0.009$, (d) $\zeta = 0.758 \pm 0.009$, (e) $\zeta = 0.78 \pm 0.01$, (f) $\zeta = 0.80 \pm 0.01$. (a) - (b) The red solid lines represent fits of the data with a Percus-Yevick structure factor [43]. (c) - (f) The vertical lines represent the expected positions of Bragg peaks for fcc (red) and bcc (dashed-green) crystalline lattices. The horizontal black lines correspond to $S(q) = 1$.

pected peak positions of microgels crystallizing in a fcc lattice. Except for the sample in panel 5(e), all the other structure factors contain additional peaks that cannot be related to an fcc lattice. The additional peaks can only be explained by the coexistence in the sample of crystals with a different lattice. While fcc is the equilibrium structure, microgel solutions can also crystallize in hexagonal or random hexagonal close-packed (hcp and rhcp, respectively) lattices since these structures are obtained by a different stacking of hexagonal planes [45] and are energetically very close to the fcc arrangement [47–49]. Therefore, we tried to reproduce the position of the additional peaks using either hcp or rhcp lattices. For both these crystalline structures, the lattice constants that reproduce the positions of the first peaks in Figures 5(c), (d) and (f), lead to positions of second peaks which are not in agreement with the measured second peaks in the structure factors. This is due to the selection rules of the Bragg reflections for these lattices [50]. Therefore, hcp and rhcp lattices have been excluded.

Softness of the microgels can lead to the formation of crystals with unexpected lattices in comparison to hard spheres, e.g. metastable body centered cubic [45, 51]. The first peak, marked by the first green dashed lines in Figures 5(c), (d) and (f), is due to the reflection from the plane $(1, 1, 0)$ in the conventional unit cell of bcc [50]. Despite the absence of higher order peaks, the presence of the bcc crystals is the most reasonable option since it leads to lattice constants comparable to the one of the fcc lattices and is in agreement with the SANS experiments presented later. Furthermore, the presence of a bcc lattice is supported by previous data in the literature related to solutions of soft microgels [45, 51]. Nevertheless, we highlight that while in Refs. [51] and [45] the bcc crystals were metastable, the extreme softness of the interaction potential between ULC microgels leads to the coexistence of two stable crystalline lattices, fcc and bcc, respectively.

III. RESPONSE OF ULTRA-LOW CROSSLINKED MICROGELS TO CROWDING: SMALL-ANGLE NEUTRON SCATTERING

To have further insight into the behavior of these ultra-soft microgels in solution, we now focus on the single microgel response to crowding. Recently, we have shown that the ultra-low crosslinked microgels are significantly compressed once embedded in a matrix of regular microgels [28]. This study revealed that ULC microgels preferentially deswell, in contrast to microgels synthesized with the addition of a crosslinker agent that show a strong interpenetration of their neighbors [28]. The different response depends both on the difference in bulk moduli between the ultra-low crosslinked and the regular microgels, but also on their different internal structures [27, 28]. Here the response of ULC microgels embedded in a matrix of deuterated ($[C_6D_3H_8NO]_n$), but otherwise

identical, ULC microgels has been studied. The use of a matrix of deuterated microgels is essential to measure the single microgel signal, where $I(q) \propto P(q)$, in crowded environment by means of small-angle neutron scattering (SANS) with contrast variation. The measurements have been performed on D11 instrument [52] at the Institut Laue-Langevin, and on the KWS-1 [53] and KWS-2 [54] instruments operated by JCNS at the Heinz Maier-Leibnitz Zentrum (*Supplemental Material*). In contrast to other studies [18, 28, 31, 55, 56], here it was necessary to use a deuterated monomer with only 3 atoms of deuterium and not 7. The reason for this is that in the D7-pNIPAM the isopropyl group of NIPAM is deuterated and consequently the cross-linking is strongly restrained [26]. As a consequence, the formation of microgels using D7-pNIPAM is precluded.

A. Experimental determination of the match point

Since we used a different monomer ($[C_6D_3H_8NO]_n$) with respect to the literature ($[C_6D_7H_4NO]_n$) [18, 28, 31, 55, 56], the match point of the deuterated ULC microgels has been determined experimentally. Figure 6(a) shows the scattered intensities of highly diluted solutions of D3-ULC microgels as a function of the scattering vector, q, suspended in various D_2O/H_2O mixtures, namely 0, 20, 50, 60, 80, and 100 wt% D_2O.

Clearly, with increasing the content of D_2O from 0 to 60 wt% the contrast get increasingly worse, as shown by Figure 6(a). For the last two mixtures, 80 and 100 wt% D_2O, the contrast is good again. Since all the solutions have the same concentration, and contain the very same microgels, the only reason for the changes in the scattered intensities is due to variations of the scattering contrast between the deuterated microgels and the solvent, $\Delta\rho$. Therefore, to find $\Delta\rho$ different scattering vectors (q_1, q_2,..., q_5) are selected (vertical lines in Figure 6(a)) and the square root of the values of the corresponding $I(q)$s at different contrast are taken for each q_i, with $i = 1 \ldots 5$ (for diluted solutions $I(q = q_i) \propto P(q = q_i) \simeq \Delta\rho^2$). These values are plotted in Figure 6(b). For the mixtures with 60, 80 and 100 wt% of D_2O the negative solutions for the contrast has been selected since the sign of $\Delta\rho$ changes when the scattering length density of the solvent crosses the match point.

For every selected q, the variation of the values of $I(q)$ depends on the variation of $\Delta\rho$. For all the chosen q, a linear fit is performed. All the fits cross the zero-axes (dashed black line) in the very same point: 55.7 ± 0.3 wt% D_2O that is the scattering length density of the deuterated ULC microgels. The samples for SANS with contrast variation have been prepared in this solvent. The scattering length density obtained experimentally is 3.137×10^{-6} Å^{-2}. The experimental value is very close to the theoretical value of 2.949×10^{-6} Å^{-2} calculated from the scattering lengths of the atoms composing the deuterated monomer [57]. The difference between the two values can be due to the incorporation of fragments of the initiators or to impurities in the deuterated monomer or solvent.

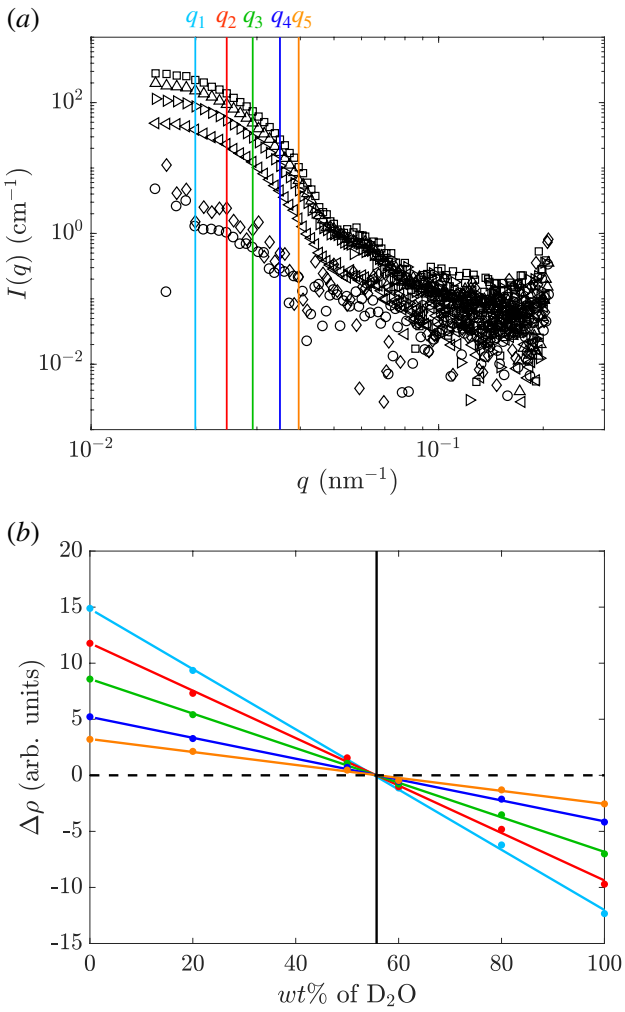

FIG. 6. (a) SANS intensity, $I(q)$, as a function of the scattering vector, q, of the deuterated-ULC microgels probed at 20.0 ± 0.1 °C suspended in D_2O/H_2O mixtures with: 100 wt% D_2O (upside triangles); 80 wt% D_2O (left-side triangles); 60 wt% D_2O (circles); 50 wt% D_2O (diamonds); 20 wt% D_2O (right-side triangles); 0 wt% D_2O (squares). The colored vertical solid lines represent fixed q used to extract the contrast in panel (b). (b) Scattering length density contrast, $\Delta\rho$, as a function of the wt% of D_2O in the solvent. The different colors corresponds to the different q chosen in panel (a) to extract the contrast. The solid lines represent linear fits of the data. The dashed black horizontal line shows the zero contrast line. The black solid vertical line represent the match point of the deuterated ULC microgels: 55.7 ± 0.3 wt% D_2O.

B. Form factor analysis in crowded environments

The volume fraction of the hydrogenated ULC microgels, ζ_H, is kept constant and equals 0.080 ± 0.003 in all

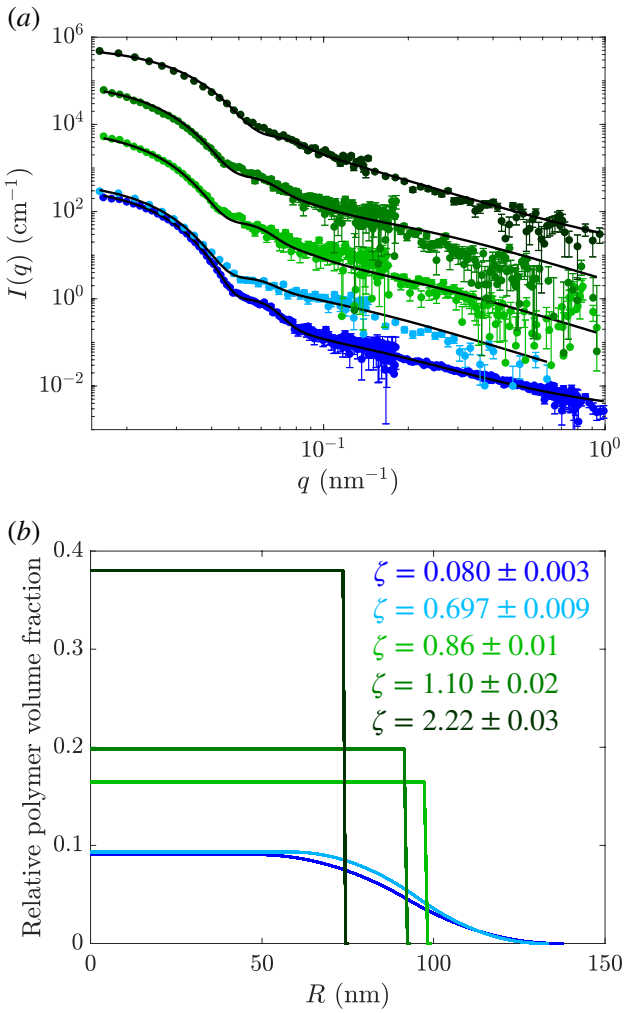

FIG. 7. (a) SANS intensity, $I(q)$, versus scattering vector, q, of the ultra-low crosslinked hydrogenated microgels. Data are shifted in the y-direction for clarity. (b) Radial distribution of the relative polymer volume fraction as obtained by fits of the curves in (a) using the model of Ref. [58]. In panel (a), the concentrations from bottom to top are: $\zeta = 0.080 \pm 0.003$; 0.697 ± 0.009; 0.86 ± 0.01; 1.10 ± 0.02; 2.22 ± 0.03. All the measurements were performed at $T = 20.0 \pm 0.01\,^{\circ}$C. The colors and concentrations in panel (b) correspond to those in panel (a).

the samples measured with SANS with contrast variation. The generalized volume fraction of the deuterated microgels composing the matrix where the hydrogenated ULC microgels are embedded, ζ_D, covers a range of concentrations between 0 and 2.14 ± 0.03. Consequently, the total generalized volume fraction, $\zeta = \zeta_H + \zeta_D$, covers a concentration range between 0.08 and 2.22 ± 0.03.

The data in Figure 7(a) (and in Figure S5(a)) are proportional to the form factors of the hydrogenated ULC microgels measured by SANS. The $I(q)$s in Figure 7 are shifted in the y-direction for clarity. The data are fitted using the model for a fuzzy-sphere [58, 59] (black solid lines), which has been shown to reproduce the form factors of ULC microgels [27, 28], therefore, this model has been chosen instead of newly developed routine for the data fitting [60, 61]. The characteristic lengths of the microgels (total radius, R_{SANS}, core radius, R_c, and length of the fuzzy shell, 2σ) obtained from the fits of the data are used to plot the radial distribution of the relative polymer volume fraction within the microgel shown in Figure 7(b) (and in Figure S5(b)). The parameters obtained from the fits, together with the mash size ξ and the size polydispersity σ_p are shown in Table I.

The blue symbols in Figure 7(a) represent the form factors of the hydrogenated ULC microgels in the dilute condition ($\zeta \leq 0.080 \pm 0.003$), i.e. without the addition of deuterated ULC microgels. The total radius in the swollen state, at $20.0 \pm 0.1\,^{\circ}$C, is 136 ± 3 nm. This value is in agreement with the value of the hydrodynamic radius of the ULC microgels ($R_h = 138.3 \pm 0.6$ nm) obtained from dynamic light scattering measurements of diluted solutions analyzed with second cumulant analysis [62, 63]. The size polydispersity and the mesh size are $\sigma_p = 9.5 \pm 0.7\%$ and $\xi = 12 \pm 2$ nm.

TABLE I. Generalized volume fractions, ζ, and fitting parameters as obtained from the fit of the SANS data. All the samples reported in the table have been measured at constant temperature ($20.0 \pm 0.01\,^{\circ}$C). The corresponding fits and radial distributions are shown in Figures 7 and S5.

ζ	R_{SANS} (nm)	R_c (nm)	2σ (nm)	ξ (nm)	σ_p (%)
0.080 ± 0.003	136±3	48 ± 1	88±2	12±2	9.5±0.7
0.593 ± 0.007	135±3	53 ± 1	81±2	12±2	11±1
0.661 ± 0.008	133±4	59 ± 2	74±2	13±1	10.9±0.9
0.697 ± 0.009	132±4	58 ± 1	74±3	13±1	10.1±0.6
0.750 ± 0.009	116±4	78 ± 2	38±2	12±1	14.0±0.9
0.79 ± 0.01	105±4	88 ± 1	16±3	12±1	13.4±0.9
0.86 ± 0.01	98±2	97 ± 1	-	7±1	14±1
0.91 ± 0.01	98±1	97 ± 1	-	6±2	14±1
0.98 ± 0.01	94±2	93 ± 1	-	5±2	15±1
1.10 ± 0.02	92±1	92 ± 1	-	6±1	16±2
1.29 ± 0.02	90±3	90 ± 1	-	5±1	18±2
1.66 ± 0.02	72±3	72 ± 1	-	4±1	17±2
2.22 ± 0.03	70±4	70 ± 1	-	4±1	16±1

When the concentration of the deuterated ULC microgels increases, a shift of the oscillation of the form factors can be observed in Figure 7(a). The oscillation of the form factor of the hydrogenated microgels in the dilute condition is between 5 and $8{\cdot}10^{-2}$ nm^{-1}, blue symbols in the bottom curve. In contrast, the oscillation of the form factor for the sample at the highest concentration we measured, $\zeta = 2.22 \pm 0.03$, appears between 7 and $9{\cdot}10^{-2}$ nm^{-1}, dark green symbols in the top curve. Such a shift is compatible with a change in size/architecture of the microgels as a consequence of the increased con-

centration. The fits of the data for all the ζ measured confirms this and the results are reported in Table I. The additional curves and fits are reported in Figure S5 in the *Supplemental Material*.

The hydrogenated ULC microgels embedded in a matrix of deuterated-, but otherwise identical, ULC microgels, maintain their size, almost unchanged up to a concentration of $\zeta = 0.697 \pm 0.009$. Not only the total size, but also all the characterizing lengths of the microgel's internal structure (R_c, 2σ, ξ) are virtually the same, within the experimental errors. The radial profiles are shown in Figure 7(b) according to the values reported in Table I. As can be seen, the radial profiles at concentrations $\zeta \lesssim 0.7$ are all virtually the same, Figures 7(b) and S5 in the *Supplemental Material*. This means that the ULC microgels are not compressed for moderate concentrations. This behavior is consistent with what is observed in the literature: microgels with comparable bulk moduli preferentially interpenetrate with their neighbors [28, 31] or facets maintaining their volume constant [32, 64] at moderate packing fractions.

When $\zeta = 0.750 \pm 0.009$ the fit of the data shows that the ULC microgels are compressed and the radius is 116±4 nm, Table I. This compression is mainly due to the compression of the fuzzy external shell that decreases its length to 38±2 nm, almost half of the length with respect to the previous fits. A further increase in concentration leads to a more pronounced collapse of the ULC microgels and at $\zeta = 0.86 \pm 0.01$, the external fuzzy shell is completely collapsed, Figures 7(b). For $\zeta > 0.80$, in Table I the length of the fuzzy shell are not indicated since the fits lead to values lower than 1 nm which is below the SANS resolution.

With increasing ζ, a constant decrease of the radius of the microgel is observed. This decrease holds until $\zeta > 1.69$. Above this value, the radii of the microgels seem to reach a constant value of $\approx$ 70 nm. This is shown in the curves corresponding to $\zeta = 1.10 \pm 0.02$ and $\zeta = 2.22 \pm 0.03$ in Figures 7(b). The complete variation of the radial profiles for all the samples measured is shown in Figure S5(b).

C. Deformation and apparent polydispersity

An important point is that our model is assuming a spherical symmetry for the microgels. Nevertheless, super-resolved microscopy has shown that for other microgels, larger than those we are using in this study, faceting and deformations arise at high packing fraction [32, 65]. As it has been shown previously for nanoemulsion droplets, an increase of the fitting parameter related to the polydispersity is consistent with the deformation, and the consequent loss, of spherical symmetry [66]. Therefore, at high concentrations, this fitting parameter has to be interpreted as an apparent size polydispersity that accounts for the faceting of the scattering object.

Figure 8 shows the increase of the parameter σ_p as a function of ζ. We think that the increase in the (apparent) polydispersity observed in our samples for $\zeta > 0.74$ can be explained by the partial faceting of the ULC microgels. It should also be taken into account that the polymeric network of the ULC microgels does not possess a well-defined gradient of crosslinker. This leads to a large variation in the bulk moduli between different ULC microgels, which in two dimensions has been shown to be responsible for the suppression of crystallization [27]. This fact, together with the observation that in bulk the softest microgels deswell at lower concentrations with respect to those with slightly larger bulk moduli [18, 21, 64], can also be the reason for the trend of the (apparent) polydispersity in Table I. Nevertheless, this increase in the (apparent) polydispersity is not suppressing the crystallization, as shown by the sample at $\zeta = 0.750 \pm 0.009$ in Figure 1(b).

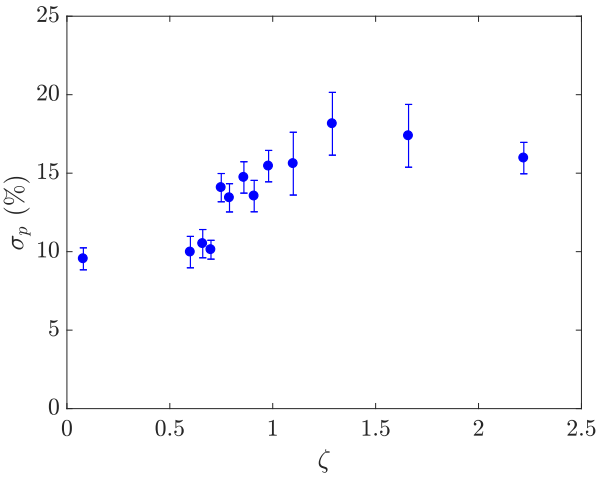

FIG. 8. Values of the fitting parameter σ_p as obtained from the fits in Figures 7 and S5 versus the generalized volume fraction.

D. Estimation of the volume fraction ϕ

A general problem when dealing with soft deformable microgels is to access the real volume fraction, ϕ, that is the real volume occupied by the microgels in solution, and not the generalized volume fraction that does not account for osmotically-induced size change. To address this problem, we can use the data on the size change of the microgels obtained with SANS with contrast variation. Nevertheless, as discussed in section III C, the observed decrease in size for $\zeta \gtrsim 0.74$ is accompanied by an increase in the parameter describing the polydispersity indicating that the microgels are deviating from a spherical shape. This means that we cannot use the values of R_{SANS} to compute reliable values for ϕ for $\zeta \gtrsim 0.74$ since in this region deformation plays a role.

Nevertheless, we can compute the volume fraction

for lower concentrations, in this case we have: $\phi = \zeta(R_{SANS}(\zeta)/R_{SANS}(\zeta = 0.080))^3$. The values for ϕ are reported in Table S5.

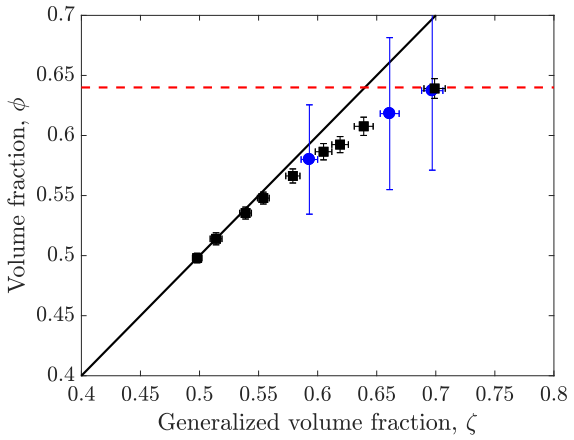

FIG. 9. Values of the volume fraction ϕ computed using the sizes for the hydrogenated ultra-low crosslinked microgels obtained by SANS versus the generalized volume fraction ζ. Circles represent samples composed of a mixture of deuterated and hydrogenated microgels while the squares represent samples composed of hydrogenated microgels only. The solid black line corresponds to $\phi = \zeta$ while the dashed red line represents the random close packing limit for hard spheres, $\phi_{rcp} = 0.64$.

Figure 9 shows the course of the calculated ϕ versus ζ determined experimentally using the weight concentration of microgel in the solution and the conversion constant obtained from the viscosimetry measurements. As can be seen for low concentrations, $\zeta \lesssim 0.54$, the data follow the line $\phi = \zeta$, solid black line. This means that the microgels do not change size, i.e. that the bulk modulus of the microgels in solution is larger than the solution osmotic pressure [18, 25]. Then, at $\zeta > 0.54$, the data starts to deviate from this law indicating that osmotic-deswelling begins. It should be noted, the change in size happens well before the direct contact between the microgels ($\phi_{rcp} = 0.64$), as already reported in the literature [18, 21, 25, 67]. Finally, with increasing concentration the data seem to flatten at the value of the random close packing for hard spheres, $\phi = 0.64$, dashed red line in Figure 9. This is consistent with the fact that, once the concentration rises more, the microgels also have to change their shape to continue to fit in the available volume. The consequence of this is the increase of the parameter describing the polydispersity, as discussed in section III C. Another point to notice is that crystals do not form for $\phi < 0.64$, this is in agreement with previous studies made on soft ionic microgels, where it was observed that softer microgels crystallize at higher packing fractions (not generalized), with respect to harder microgels and hard spheres [12].

IV. COMPARISON BETWEEN SMALL ANGLE X-RAY AND NEUTRON SCATTERING

We notice that the crystals in the solution composed of a mixture of deuterated and hydrogenated ULC microgels appear at the same concentrations as the samples composed only by hydrogenated ULC microgels, i.e. the phase behavior of the different solutions is the same. This further confirms that the deuterated microgels are identical to the hydrogenated ULC microgels except for the presence of the three atoms of deuterium per NIPAM monomer. This allows us to directly compare the data we obtained from SAXS and from SANS.

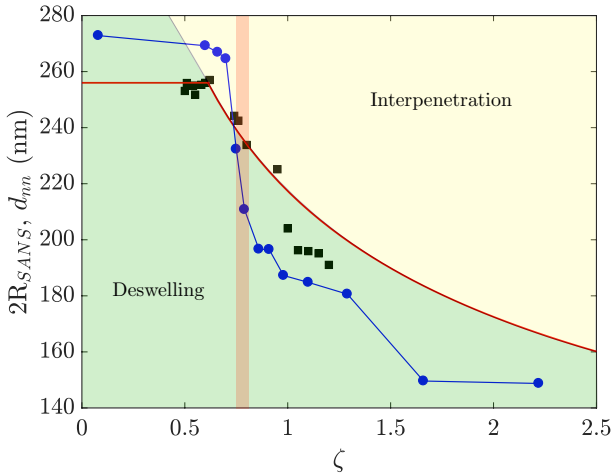

FIG. 10. Particle diameter $2R_{SANS}$ (measured with SANS, blue circles) and nearest-neighbor distance d_{nn} (measured with SAXS, black solid squares) vs. generalized volume fraction ζ for ultra-low crosslinked microgel solutions. Red curve is a fit of the d_{nn} data for $0.60 \gtrsim \zeta \gtrsim 1$ to the function $c\zeta^{-1/3}$ with fit parameter c.

Figure 10 compares the nearest neighbors distance obtained from SAXS, d_{nn} (black squares), with the diameter of the hydrogenated ULC microgels embedded in the matrix of deuterated ultra-low crosslinked microgels measured by SANS with contrast variation, $2R_{SANS}$ (blue circles).

Let us consider first the behavior of d_{nn} as a function of the generalized volume fraction ζ. For $\zeta \lesssim 0.60$ the nearest neighbor distance is constant: the red horizontal line is drawn at the average value $\langle d_{nn} \rangle = 256$ nm. For $0.60 \gtrsim \zeta \gtrsim 1$, the data decrease as a function of $\zeta^{-1/3}$. This behavior is consistent with an isotropic deswelling of the particles as reported in the literature [13, 18, 31, 56]. The red line in Figure 10 is a fit of the data $0.60 \gtrsim \zeta \gtrsim 1$. For $\zeta \gtrsim 1$, the data show a compression that has a stronger dependence on ζ. This can be explained by the deformation of the particles in response to the overcrowding.

Now let us focus on the values of the diameter of the ULC microgels. The blue circles that lie in the yellow

area of Figure 10 represent concentrations for which the ULC microgels have a diameter larger than the center-to-center distance between the microgels in the solution: at these concentrations the microgels interpenetrate each other and maintain an external fuzziness (Figures 7(b) and S5(b) and Table I).

In contrast, the blue circles in the green area of Figure 10 represent solutions at a ζ where the diameter of the ultra-low crosslinked microgels is smaller than the center-to-center distance between two neighbors, i.e. the microgels are deswollen and in contact with each other without (or with very limited) interpenetration and external fuzzy shell (Figures 7(b) and S5(b) and Table I).

As mentioned above, when microgels with different bulk moduli are mixed together the softest microgels deswell first with respect to microgels with slightly larger bulk moduli [18]. This mechanism allows for crystals to form at higher polydispersity with respect to hard spheres [13, 21, 64]. Ultra-low crosslinked microgels do not have a well defined crosslink distribution, due to the absence of crosslinking agent during the synthesis. Consequence of this are the observed large differences in stretching of ULC microgels once adsorbed at the interfaces which reveal a significant variation of bulk moduli between different ULC microgels [24, 25, 27, 67].

The red rectangular area in Figure 10 represents the range of concentrations where the coexistence between stable bcc and fcc lattices has been observed. As can be seen in this region, we register the passage from interpenetration to deswelling. The two mechanisms are competing. In this region, ULC microgels with softer bulk moduli have a collapsed fuzzy shell while ULC microgels with a larger number of crosslinks or with a different topology of the network maintain a fuzzy periphery. This fact can be used to explain the variation of σ_p versus ζ in Figure 8 but also to understand the coexistence between bcc and fcc lattices.

Deswollen ULC microgels are similar to spheres without fuzziness. These systems obey the maximum packing fraction rule: to increase the configurational entropy of the system, they maximize the packing fraction due to pure excluded-volume interactions. For spheres in bulk, the maximum packing fraction is reached in a fcc lattice [47, 68].

In contrast, particles with a less defined - fuzzy - periphery, as the swollen ULC microgels, maximize their configurational entropy by increasing the contacts between neighbors [69]. This criterion has to be fulfilled since the particle-to-particle interaction for these systems scales with the contact area. In this scenario, the most efficient structure to maximize the contact area between neighbors is the bcc (or A15) lattice [69, 70].

In the region of transition between fuzzy- and collapsed ultra-low crosslinked microgels, in the red area of Figure 10, there are (deswollen) microgels which maximize their configurational entropy following the maximum packing fraction rule and other microgels (with external fuzziness) which maximize their configurational entropy maximizing the contact area with their neighbors. The collapsed microgels form fcc crystals while the still fuzzy microgels form bcc crystals.

The coexistence in the solutions of microgels with slightly different sizes, due to the more or less pronounced collapse of their external fuzzy shell, is also consistent with the absence of higher Bragg reflections observed in the SAXS experiments. The crystals that these microgels form have different structures, fcc or bcc, but also incorporate a significant number of defects, due to the size mismatch. These defects have been recognized as the reason for the absence of a second ring of Bragg reflection [13, 41].

V. CONCLUSIONS

In this study, the phase behavior of super-soft spheres has been characterized. Our model system for super-soft spheres consists of solutions of ultra-low crosslinked microgels. These microgels incorporate the lowest number of charges compared to microgels synthesized with the addition of crosslinker agents. Therefore, the effects of the counterions on the solution osmotic pressure [12, 18, 67] and, consequently, on the microgel phase behavior [13, 24], are limited. This allows to study the phase behavior of soft spheres as a function of the packing fraction only.

The phase behavior presents the expected liquid-to-crystal transition and the formation of dense disordered states. The freezing and melting points are shifted to higher packing fraction, $\zeta_f = 0.717 \pm 0.09$ and $\zeta_m = 0.744 \pm 0.009$, respectively. These values are significantly larger as compared to the typical values of $\zeta_f = 0.56 - 0.58$ and $\zeta_m = 0.61$ observed for other solutions of almost neutral microgels [13, 19, 34, 36, 37]. The shift of the boundaries of the liquid-to-crystal transition in our system is consistent with the prediction of computer simulation for particles interacting with very soft potentials [20].

The complex interplay between compression and interpenetration of the ultra-low crosslinked microgels has been directly probed combining small-angle X-ray and neutron scattering with contrast variation to access both the particle-to-particle distance and the shape of the single microgels. These measurements reveal the coexistence between fcc and bcc stable lattices. The latter was observed as metastable lattice in solutions of stiffer microgels [45, 51] or for nucleation of crystals of weakly charged colloids [71]. The stable bcc crystals are due to the fact that in the concentration range where crystals form, some of the ultra-low crosslinked microgels maintain their fuzzy shell partially swollen. Therefore, being their interaction dependent on the contact area with their neighbors, their configurational entropy is maximized by a bcc lattice [69].

Due to the easy synthetic protocol and the fine control over the size and size polydispersity, ultra-low crosslinked

microgels represent valid model systems for super-soft spheres to investigate the role of softness on the crystallization process. They can be used in future to investigate the prediction of the nucleation rate for soft spheres and compare it to the prediction for hard spheres [5, 72]. Furthermore, ultra-low crosslinked microgels can be used to investigate the glass and jammed states. We recently demonstrated that they can form both glass and jammed samples [29]. Even in this case, the advantage of using ULC microgels over other microgels is that the effects of charges and of osmotic deswelling are minimized.

ACKNOWLEDGMENTS

Data availability Authors are thankful to Dr. A. Menzel and to the EUSMI program for the help with the measurements performed on the cSAXS beamline of the Swiss Light Source, Paul Scherrer Institut. Financial support of the Deutsche Forschungsgemeinschaft within SFB 985 - Functional Microgels and Microgel Systems, the International Helmholtz Research School of Biophysics and Soft Matter (IHRS BioSoft) is gratefully acknowledged. All the data used for this paper are available, under request, PID: 21.11102/c56fba01-afda-11ea-afb2-e41f1366df48. This work is based upon experiments performed at the D11 instrument at the Institut Laue-Langevin (ILL), Grenoble, France (doi.ill.fr/10.5291/ILL-DATA.9-10-1580) and at the KWS-1 and KWS-2 instruments operated by JCNS at the Heinz Maier-Leibnitz Zentrum (MLZ), Garching, Germany. We also acknowledge the use of the free SasView software (http://www.sasview.org/) for fitting the Perkus-Yevik model and the use of FitIt! for the fits of the form factors (www.github.com/ovirtanen/fitit).

[1] W. Hoover and F. Ree, J. Chem. Phys. **49**, 3609 (1968).
[2] M. Baus, Journal of statistical physics **48**, 1129 (1987).
[3] D. Frenkel, Journal of Physics: Condensed Matter **6**, A71 (1994).
[4] P. N. Pusey and W. van Megen, Nature **320**, 340 (1986).
[5] U. Gasser, E. R. Weeks, A. Schofield, P. N. Pusey, and D. A. Weitz, Science **292**, 2580 (2001).
[6] H. H. von Grünberg, P. Keim, K. Zahn, and G. Maret, Phys. Rev. Lett. **93**, 255703 (2004).
[7] U. Gasser, Journal of Physics: Condensed Matter **21**, 203101 (2009).
[8] X. Ma, Z. S. Davidson, T. Still, R. J. S. Ivancic, S. S. Schoenholz, A. J. Liu, and A. G. Yodh, Phys. Rev. Lett. **122**, 028001 (2019).
[9] R. Pelton and P. Chibante, Colloids and Surfaces **20**, 247 (1986).
[10] M. Muluneh and D. A. Weitz, Phys. Rev. E **85**, 021405 (2012).
[11] D. Gottwald, C. Likos, G. Kahl, and H. Löwen, Physical review letters **92**, 068301 (2004).
[12] M. Pelaez-Fernandez, A. Souslov, L. A. Lyon, P. M. Goldbart, and A. Fernandez-Nieves, Phys. Rev. Lett. **114**, 098303 (2015).
[13] A. Scotti, U. Gasser, E. S. Herman, J. Han, A. Menzel, L. A. Lyon, and A. Fernandez-Nieves, Phys. Rev. E **96**, 032609 (2017).
[14] M. Cloitre, R. Borrega, and L. Leibler, Physical Review Letters **85**, 4819 (2000).
[15] M. Cloitre, R. Borrega, F. Monti, and L. Leibler, Physical review letters **90**, 068303 (2003).
[16] S. P. Meeker, R. T. Bonnecaze, and M. Cloitre, Physical Review Letters **92**, 198302 (2004).
[17] M. Stieger, J. S. Pedersen, P. Lindner, and W. Richtering, Langmuir **20**, 7283 (2004).
[18] A. Scotti, U. Gasser, E. S. Herman, M. Pelaez-Fernandez, L. A. Lyon, and A. Fernandez-Nieves, Proc. Natl. Acad. Sci. USA **113**, 5576 (2016).
[19] H. Senff and W. Richtering, J. Chem. Phys. **111**, 1705 (1999).
[20] R. Agrawal and D. A. Kofke, J. Phys. Chem. B **85** (1995).
[21] A. S. J. Iyer and L. A. Lyon, Angew. Chem. Int. Ed. **48**, 4562 (2009).
[22] D. Frenkel, Nature **460**, 465 (2009).
[23] W. McPhee, K. C. Tam, and R. Pelton, Journal of colloid and interface science **156**, 24 (1993).
[24] M. Urich and A. R. Denton, Soft matter **12**, 9086 (2016).
[25] U. Gasser, A. Scotti, and A. Fernandez-Nieves, Physical Review E **99**, 042602 (2019).
[26] M. Brugnoni, A. C. Nickel, L. C. Kröger, A. Scotti, A. Pich, K. Leonhard, and W. Richtering, Polymer Chemistry **10**, 2397 (2019).
[27] A. Scotti, S. Bochenek, M. Brugnoni, M. A. Fernandez-Rodriguez, M. F. Schulte, J. E. Houston, A. P. H. Gelissen, I. I. Potemkin, L. Isa, and W. Richtering, Nature Communications **10**, 1418 (2019).
[28] A. Scotti, A. R. Denton, M. Brugnoni, J. E. Houston, R. Schweins, I. I. Potemkin, and W. Richtering, Macromolecules **52**, 3995 (2019).
[29] A. Scotti, M. Brugnoni, C. G. Lopez, S. Bochenek, J. J. Crassous, and W. Richtering, Soft Matter **16**, 668 (2020).
[30] M. F. Schulte, A. Scotti, M. Brugnoni, S. Bochenek, A. Mourran, and W. Richtering, Langmuir **35**, 14769 (2019).
[31] P. S. Mohanty, S. Nöjd, K. v. Gruijthuijsen, J. J. Crassous, M. Obiols-Rabasa, R. Schweins, A. Stradner, and P. Schurtenberger, Scientific Reports **7**, 1487 (2017).
[32] G. M. Conley, C. Zhang, P. Aebischer, J. L. Harden, and F. Scheffold, Nature communications **10**, 2436 (2019).
[33] J. Mattsson, H. M. Wyss, A. Fernandez-Nieves, K. Miyazaki, Z. Hu, D. R. Reichman, and D. A. Weitz, Nature **462**, 83 (2009).
[34] S. B. Debord and L. A. Lyon, J. Phys. Chem. B **107**, 2927 (2003).
[35] G. K. Batchelor, J. Fluid Mech. **83**, 97 (1977).
[36] S. Paulin, B. J. Ackerson, and M. Wolfe, Journal of colloid and interface science **178**, 251 (1996).
[37] D. Paloli, P. S. Mohanty, J. J. Crassous, E. Zaccarelli, and P. Schurtenberger, Soft Matter **9**, 2927 (2013).
[38] M. J. Bergman, N. Gnan, M. Obiols-Rabasa, J.-M. Mei-

jer, L. Rovigatti, E. Zaccarelli, and P. Schurtenberger, Nature communications **9**, 1 (2018).
[39] F. Scheffold, P. Díaz-Leyva, M. Reufer, N. B. Braham, I. Lynch, and J. L. Harden, Physical review letters **104**, 128304 (2010).
[40] M. Rubinstein, R. H. Colby, *et al.*, *Polymer physics*, Vol. 23 (Oxford university press New York, 2003).
[41] S. Martin, G. Bryant, and W. van Megen, Physical review letters **90**, 255702 (2003).
[42] J. Liu, H.-J. Schöpe, and T. Palberg, Particle & Particle Systems Characterization: Measurement and Description of Particle Properties and Behavior in Powders and Other Disperse Systems **17**, 206 (2000).
[43] J. K. Percus and G. J. Yevick, Phys. Rev. **110**, 1 (1958).
[44] J. Wu, B. Zhou, and Z. Hu, Phys. Rev. Lett. **90**, 048304 (2003).
[45] U. Gasser, J.-J. Lietor-Santos, A. Scotti, O. Bunk, A. Menzel, and A. Fernandez-Nieves, Phys. Rev. E **88** (2013).
[46] M. S. Wertheim, Phys. Rev. Lett. **10**, 321 (1963).
[47] D. Frenkel and A. J. Ladd, The Journal of chemical physics **81**, 3188 (1984).
[48] P. Bolhuis and D. Frenkel, Phys. Rev. Lett. **72**, 2211 (1994).
[49] S. Pronk and D. Frenkel, J. Chem. Phys. **110**, 4589 (1999).
[50] C. Kittel, P. McEuen, and P. McEuen, *Introduction to solid state physics*, Vol. 8 (Wiley New York, 1996).
[51] P. Mohanty and W. Richtering, J. Phys. Chem. B **112**, 14692 (2008).
[52] P. Lindner and R. Schweins, Neutron News **21**, 15 (2010).
[53] A. V. Feoktystov, H. Frielinghaus, Z. Di, S. Jaksch, V. Pipich, M.-S. Appavou, E. Babcock, R. Hanslik, R. Engels, G. Kemmerling, *et al.*, Journal of applied crystallography **48**, 61 (2015).
[54] A. Radulescu, V. Pipich, H. Frielinghaus, and M.-S. Appavou, in *Journal of Physics: Conference Series*, Vol. 351 (IOP Publishing, 2012) p. 012026.
[55] U. Gasser, J. S. Hyatt, J.-J. Lietor-Santos, E. S. Herman, L. A. Lyon, and A. Fernandez-Nieves, J. Chem. Phys. **141** (2014).
[56] S. Nöjd, P. Holmqvist, N. Boon, M. Obiols-Rabasa, P. S. Mohanty, R. Schweins, and P. Schurtenberger, Soft Matter **14**, 4150 (2018).
[57] F. S. Varley, Neutron news **3**, 29 (1992).
[58] M. Stieger, W. Richtering, J. Pedersen, and P. Lindner, J. Chem. Phys. **120**, 6197 (2004).
[59] I. Berndt, J. S. Pedersen, and W. Richtering, Journal of the American Chemical Society **127**, 9372 (2005).
[60] M. Cors, L. Wiehemeier, Y. Hertle, A. Feoktystov, F. Cousin, T. Hellweg, and J. Oberdisse, Langmuir **34**, 15403 (2018).
[61] M. Cors, L. Wiehemeier, O. Wrede, A. Feoktystov, F. Cousin, T. Hellweg, and J. Oberdisse, Soft matter **16**, 1922 (2020).
[62] D. E. Koppel, J. Chem. Phys. **57**, 4814 (1972).
[63] W. Burchard and W. Richtering, Progr. Colloid Polym. Sci. **80**, 151 (1989).
[64] I. Bouhid de Aguiar, T. van de Laar, M. Meireles, A. Bouchoux, J. Sprakel, and K. Schroën, Scientific Reports **7**, 10223 (2017).
[65] G. M. Conley, P. Aebischer, S. Nöjd, P. Schurtenberger, and F. Scheffold, Science Advances **3**, e1700969 (2017).
[66] F. Scheffold and T. Mason, Journal of Physics: Condensed Matter **21**, 332102 (2009).
[67] A. R. Denton and Q. Tang, The Journal of chemical physics **145**, 164901 (2016).
[68] R. Higler, J. Appel, and J. Sprakel, Soft Matter **9**, 5372 (2013).
[69] P. Ziherl and R. D. Kamien, Phys. Rev. Lett. **85**, 3528 (2000).
[70] P. Ziherl and R. D. Kamien, Journal of Physical Chemistry B **105**, 10147 (2001).
[71] S. Auer and D. Frenkel, Journal of physics. Condensed Matter **14**, 7667 (2002).
[72] S. Auer and D. Frenkel, Nature **409**, 1020 (2001).